

Chapter 8

Coupled Fracture Modelling with RFPA



Gen Li, Chun'an Tang, Zhengzhao Liang, and Lianchong Li

Abstract In order to investigate the hydraulic fracture development of the rock and simulate the cracks driven by fluid flow in rocks, a statistical meso-damage mechanical method is developed, based on the statistical and continuum flow-stress-damage model and the finite element method. The constitutive law of this model considers strength and stiffness degradation, stress-dependent permeability for the pre-peak stage, and deformation dependent permeability for the post-peak stage. The damage evolution and accumulation of mesoscopic representative volume element is used to reflect the macroscopic failure characteristics of rock. Three coupled hydro-mechanical processes are considered: (1) mechanical deformation of the solid medium induced by the fluid pressure acting on the fracture surfaces and the rock skeleton, (2) fluid flow within the fracture, and (3) propagation of the fracture. The global flow, stress and strain fields are solved by the finite element method. An element represents a representative volume element, the initiation and propagation of meso-macroscopic trans-scale cracks and their interaction are manifested by removing the failed elements. The above ideas are formulated in the framework of the coupled fracture modelling, which is encoded and implemented into a self-developed software Rock Failure Process Analysis code (RFPA).

Keywords Rock fracture · Crack · Damage · Hydraulic fracture · RFPA

G. Li · C. Tang (✉) · Z. Liang
State Key Laboratory of Coastal and Offshore Engineering, Dalian University of Technology,
Dalian, China
e-mail: ligen8@dlut.edu.cn; catang@mechsoft.cn; LiangZZ@dlut.edu.cn

L. Li
School of Resources and Civil Engineering, Northeastern University, Shenyang, China
e-mail: Li_Lianchong@163.com

8.1 Background

Among the problems that are faced by rock and civil engineers, there is nothing more challenging than the characterization of fluid flow through fracturing rocks, especially in highly stressed rocks (Tang et al. 2002). Based on the underlying mechanical and hydraulic natures of the basic components of a rock mass, a large number of numerical models for flow-stress or flow-strain coupling analysis have been developed in recent years (Shen et al. 2012; Zhu et al. 2008; Tang and Kaiser 1998; Zhu and Tang 2004; Ma et al. 2011; Zhao et al. 2010; Potyondy and Cundall 2004; Feng et al. 2006; Zhou and Yang 2012; Lisjak et al. 2014a, b), which can be classified into three categories:

- Discontinuum-based models. These models can directly and explicitly permit cracks development of localization and coalescence. Those discrete element method based models are dependent on the predefined flaws or network of discontinuities and limited by the state of computing technology as to the size of problem to be dealt with. Therefore these models have limited capacity in fracture modelling. Those Displacement Discontinuity Method based models can handle the fracture propagation process well, but are inflexible in dealing with the rock mass inhomogeneity.
- Continuum-based models. Depending on whether to consider the physical degradation behavior of individual microcracks, continuum-based models can be subdivided into two categories: the phenomenological models and the micromechanics-based models. The phenomenological models usually require complex constitutive laws to account for the purely macroscopic damage evolution and strength weakening of rock and could not capture the transition from the continuum to discontinuum behaviors. Therefore these models cannot reflect the complete failure process involving crack initiation, propagation and coalescence. When dealing with material deformation and fracturing process indirectly by continuum-based models, some special techniques are required to overcome the difference between the continuity state of a problem and randomness and discontinuity of crack propagation under the theoretical framework. As a result, various new methods have been continuously developed. The continuum-based numerical methods are relatively mature and can be easily implemented. It is an alternative to explicit treatment of cracking by discontinuum-based models. The continuum-based models have attracted a lot of attentions nowadays (Yuan and Harrison 2006).
- Hybrid models. Hybrid models were developed to take advantages of both continuum and discontinuum-based models. Although hybrid models could be successful in simulating internal crack propagation, and capable to reflect the main characteristics of the damage and fracturing process, the presence of pre-existing flaws (or special crack elements) is always required. Especially, the bottleneck in computational efficiency still exists.

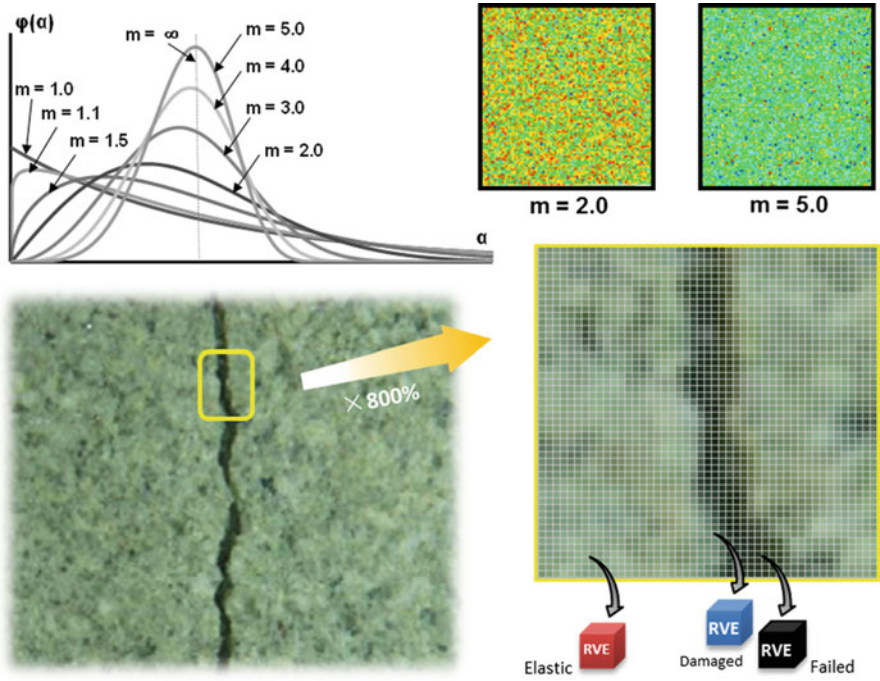


Fig. 8.2 Photo transformation from pixel to mesh (grid) for a macroscopic crack in rock and Weibull distribution

scale (Esmaili et al. 2010; Zhang et al. 2013). It means that the structural characteristics of rock at this scale are no longer prominent, while the material properties may be nearly homogeneous due to the same geological history, and the representative elementary volume (REV) contains approximately the same rock types and defects. The relevant scale is defined as meso-scale (Li and Tang 2015), and the corresponding physical REV is defined as the representative volume element (RVE) (Esmaili et al. 2010; Zhang et al. 2013).

The RVE marks transitions between scales of heterogeneity and represents natural scales for modelling, which is the smallest volume over which the average properties can be assumed homogeneous and isotropic. From a general point of view, the definition of various scales in rock media is disputable due to complex objective and subjective factors, such as the integrity of rock, the continuous-discontinuous characteristics of rock, the modeling capacity of computers, the area of interest and the importance of the project under study etc. At macro-scale, rock behaviors are dependent on both the material characteristics and the structural characteristics. Therefore, rock is heterogeneous at macro-scale, and can be described by a certain statistical distribution, as shown in Fig. 8.2. A local image of macroscopic failure in a rock sample is given in Fig. 8.2. If the local image is magnified by 800%, it is found that the continuous crack is in fact composed of many

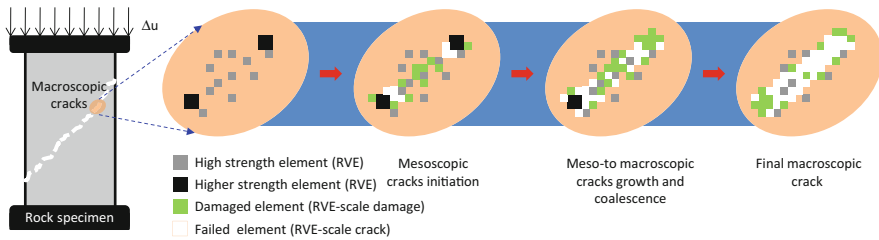


Fig. 8.3 Illustration of multi-scale crack growth process based on mesoscopic RVE-scale damage evolution

small grids in similar color. These small grids are the RVE of the image. Based on this concept, the evolution process of RVE can be represented in the framework of elasto-damage mechanics, including elastic, damage and failure states. The initiation, propagation and coalescence of cracks can be reproduced. Meanwhile, an RVE can only have one damage mode (corresponding to one damage mechanism). Its damage evolution process is a simple function of stress-strain state. The stress-strain field can be obtained from the displacement by FE modeling. In the FEM framework of continuum mechanics, no special singular element is needed, which simplifies the problem of the discontinuity since no change in the mathematical description of the model is required. The mesoscopic fracture has the minimum width of an element (i.e. RVE). The closer the mesh size to meso-scale, the stronger its ability to simulate irregular cracks and the better it can reflect the interaction between multi-scale cracks. Hence, parallel FE implementation is an effective means to enhance the space-time efficiency in numerical modeling. For failed elements, correct color is assigned so that the element color is consistent with the background color. In this way, the failed elements are removed (assigned with a zero property), and the multiscale cracks are represented. However, element removal does not mean that the element is really eliminated from the FE mesh. The interaction between meso- and macroscopic cracks (aggregation, nucleation, branching, etc.) can be considered naturally in solving the system of total stiffness matrix equation. Multiscale cracks growth process based on mesoscopic element-scale damage evolution is depicted in Fig. 8.3. In addition, in FE analysis, the failure (or damage) of each element can be assumed to be the source of an acoustic emission (AE) event because the elastic energy stored in the element is released during the failure process. Therefore, by recording the number of damaged elements and the associated amount of energy release, RFPA is capable of simulating AE activities as the AE event counts.

8.2.2 Statistical Volume Element

Based on image recognition, as shown in Fig. 8.2, the macroscopic rock can be divided into a series of regularly arranged, uniform and square mesoscopic RVEs,

the initial defects are generalized into mesoscopic equivalent RVEs by statistical homogenization, i.e. statistical volume element (SVE). A representative property of interest including elastic modulus, Poisson's ratio, and strength can be reflected by SVE. The Monte-Carlo techniques are applied to describe the spatial distribution of a certain mechanical property of SVE based on the Weibull function with threshold values (Weibull 1981) as

$$\varphi(\alpha) = \frac{m}{\alpha_0} \cdot \left(\frac{\alpha}{\alpha_0}\right)^{m-1} \cdot \exp\left(-\left(\frac{\alpha}{\alpha_0}\right)^m\right) \quad (8.1)$$

where α_0 is the scale parameter giving the characteristic value of distribution α ; m is the shape parameter describing the spatial concentration and dispersion degree of α . With increasing m , the generated data are more concentrated. In Fig. 8.2, the inhomogeneous undulation features of rock physical properties can be well reflected at the mesoscopic level by statistical function.

8.2.3 The Mesoscopic Elasto-Brittle-Damage Constitutive Law

In this section, an improved flow-stress(strain)-damage (FSD) model is presented that explicitly represents a relationship between stress(strain), damage and permeability. In RFPA3D-Parallel, isotropic conditions are considered for the hydraulic behaviour at the elemental scale. According to Darcy's law of seepage flow in porous media, the flow of a fluid (water) is governed by:

$$\nabla \left[\frac{k\rho_l g}{\mu_l} (\nabla P - \rho_l g \nabla Z) \right] = S \frac{\partial P}{\partial t} - \alpha \frac{\partial \varepsilon_v}{\partial t} \quad (8.2)$$

where k is permeability, ρ_l is fluid density, μ_l is fluid dynamic viscosity, g is gravity, P is pore fluid pressure, Z is elevation, S is storage coefficient, α is Biot's coefficient, and ε_v is volumetric strain.

The equilibrium equations and the strain-displacement relations can be expressed as

$$\frac{\partial \sigma_{ij}}{\partial x_{ij}} + f_i = 0 \quad (i, j = 1, 2, 3) \quad (8.3)$$

$$\varepsilon_{ij} = \frac{1}{2} (U_{ij} + U_{j,i}) \quad (8.4)$$

where σ_{ij} is total stress in the ij -plane, f_i is volumetric body force, ε_{ij} is strain, and U_i is solid displacement. The governing equations for the elastic deformation of an isotropic linear poroelastic medium are

$$G u_{i,jj} + \frac{G}{1-2\nu} u_{j,ji} - \alpha P_{,i} + f_i = 0 \quad (8.5)$$

where G is shear modulus.

Initially, the element is considered to be elastic; its elastic properties can be defined by Young's modulus and Poisson's ratio. The stress-strain curve of each element is considered to be linear elastic until the given damage threshold is attained. As previously mentioned, we choose the maximum tensile stress (or strain) criterion and Mohr-Coulomb criterion as damage thresholds. The tensile stress (or strain) criterion is used first to determine whether an element is damaged. If the element is not damaged in tensile mode, the Mohr-Coulomb criterion is then used to determine whether the element is damaged in shear. The sign convention used throughout this paper is that compressive stresses and strains are positive. All following equations operate on effective stresses only.

In elastic damage mechanics, the elastic modulus may degrade gradually as damage progresses, and the elastic modulus of the damaged material is defined as

$$E = (1 - D)E_0 \quad (8.6)$$

where D is the damage variable and E_0 is the elastic modulus of the undamaged material. The element and its damage are assumed to be isotropic and elastic, and therefore, E , E_0 , and D are all scalar. D ranges from zero (0.0) for the undamaged material to one (1.0) to represent full failure.

8.2.3.1 Damage Evolution of the Element in Tensional State

When the mesoscopic element is under uniaxial tension, the constitutive relationship illustrated in Fig. 8.4a is adopted. Figure 8.4a presents the uniaxial elasto-brittle damage constitutive relations with given specific residual strength.

When the tensile stress in an element reaches the tensile strength f_r , i.e., $|\sigma_3| > f_r$, the damage variable D can be calculated as

$$D = \begin{cases} 0 & \varepsilon > \varepsilon_{t0} \\ 1 - \frac{f_{tr}}{\varepsilon E_0} & \varepsilon_{tu} < \varepsilon \leq \varepsilon_{t0} \\ 1 & \varepsilon \leq \varepsilon_{tu} \end{cases} \quad (8.7)$$

where f_{tr} is the residual tensile strength, ε_{t0} is the strain at the elastic limit, which is the so-called threshold strain for tensile damage, while ε_{tu} is the ultimate tensile strain, at which the element would be completely damaged in tension.

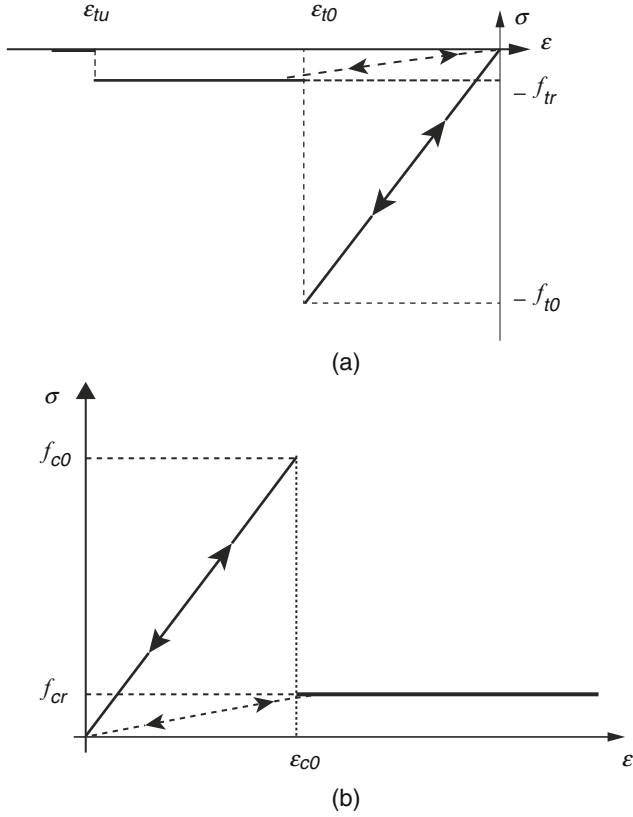


Fig. 8.4 Elastic-brittle damage constitutive law of element subject to uniaxial stress. (a) Elastic damage constitutive law of element under uniaxial tensile stress. (b) Elastic damage constitutive law of element under uniaxial compressive stress

The generalised Hooke’s law in the principal stress state can be expressed as

$$\sigma_i = \frac{E}{1 + \nu} \left[\epsilon_i + \frac{\nu}{1 - 2\nu} \epsilon_{jj} \right] \quad (i, j = 1, 2, 3) \quad (8.8)$$

From Eq. 8.8 and the maximum tensile stress criterion, one may obtain

$$E = \frac{f_t}{\frac{\epsilon_3}{1 + \nu} + \eta \epsilon_v} \quad (8.9)$$

where $\eta = \frac{\nu}{(1 + \nu)(1 - 2\nu)}$.

From Eqs. 8.6 and 8.9, the damage variable D in the triaxial stress state can be defined as

$$D = 1 - \frac{f_t}{\frac{\varepsilon E_0}{1+\nu} + \eta E_0 \varepsilon_v} \quad (8.10)$$

8.2.3.2 Damage Evolution of the Element in Compressive State

To describe the element damage under compressive or shear stress conditions, we use the Mohr-Coulomb criterion as the second damage criterion

$$\sigma_1 - \sigma_3 \geq f_c \quad (8.11)$$

where f_c is the uniaxial compressive strength, $\psi = \frac{1+\sin\phi}{1-\sin\phi}$ and ϕ is the internal friction angle.

Corresponding to the damage evolution laws in tension, similar damage evolution laws are given in Fig. 8.4b when the element is under uniaxial compression and damaged in shear according to the Mohr-Coulomb criterion. The damage variable under uniaxial compression is described as

$$D = \begin{cases} 0 & \varepsilon < \varepsilon_{c0} \\ 1 - \frac{f_c}{\varepsilon E_0} & \varepsilon \geq \varepsilon_{c0} \end{cases} \quad (8.12)$$

When an element is under a triaxial stress state, from Eqs. 8.8 and 8.11, one can obtain

$$E = \frac{f_c}{\frac{\varepsilon_1}{1+\nu} + \eta \varepsilon_v - \left(\frac{\varepsilon_3}{1+\nu} + \eta \varepsilon_v \right) \psi} \quad (8.13)$$

Using Eqs. 8.6 and 8.13, the damage variable D in the triaxial stress state can be defined as

$$D = 1 - \frac{f_c}{E_0 \left[\frac{\varepsilon_1}{1+\nu} + \eta \varepsilon_v - \left(\frac{\varepsilon_3}{1+\nu} + \eta \varepsilon_v \right) \psi \right]} \quad (8.14)$$

In this model, the element may gradually damage according to the above elastic damage constitutive relationship. Only elements whose ultimate tensile strain has been attained are displayed as cracks with black color in the post-processing figures. Elements whose shear stress has been attained are displayed as cracks with black color also. Both tensile damage and shear damage leads to the degradation of elements, but tensile damage is considered to be the direct cause of crack initiation. One of the main features of this type of model is that there is no need for a pre-existing crack to simulate the crack initiation and propagation. This approach

to simulating cracks is similar to a smeared crack model, i.e., no special singular element is used, which has the advantage of leaving the mesh topology untouched. A similar principle has been addressed and applied to modelling concrete damage (Pietruszczak and Xu 1995; Pearce et al. 2000). The method is, mathematically, a linear and continuum mechanics method for numerically processing nonlinear and discontinuum mechanics problems in rock failure. With the advance in the performance of computers, an increasing number of researchers attempt to use the similar principle to solve discontinuous problems through continuum mechanics (Fang and Harrison 2002; Zhu and Tang 2004; Ma et al. 2011).

8.2.3.3 Permeability Variation of the Element with Damage

When an element of rock undergoes dilatancy due to the degradation of strength and stiffness, its hydraulic properties will change. Experimental results indicate that dilatancy leads to an increase in permeability. These changes in hydraulic properties can be directly related to either stress or strain (Stormont and Daemen 1992; Zhu and Wong 1997; Otto Schulze et al. 2001).

Most of the theories regarding stress-induced variations of permeability refer to the pre-failure phase. During elastic deformation, rock permeability decreases when the rock compacts and increases when the rock extends. The permeability variation for an intact rock element (when $D = 0$) in the elastic state can be described as (Li and Wu 1997; Tang et al. 2002)

$$k_e = k_0 \exp[-\beta(\sigma_{ii}/3 - \alpha P)] \quad (8.15)$$

where k_0 is the initial permeability of the rock element, β is the coupling coefficient, and $\sigma_{ii}/3$ is the average total stress. In RFPA3D, Eq. 8.15 is employed to represent the influence of stress on permeability for an intact rock element.

In the post-peak stage, rock elements undergo both instantaneous strength degradation and volumetric expansion. Although many experiments have shown that there is a clear correlation between volumetric dilatancy and the increase in permeability in brittle rocks at the micro-scale, it is generally difficult to characterise small-scale elements accurately and then relate their properties to macroscopic hydraulic properties that are of practical interest (Shao et al. 2005; Jaeger et al. 2007). In the FSD model, all the constitutive laws are based on a single mesoscopic element. This degradation is physically manifested as the development of fractures, and this is one of the important concepts addressed in the improved FSD model used in RFPA3D. To apply appropriate post-peak hydraulic characteristics, the use of a strain-based formulation for the permeability variation may be more suitable (Susan et al. 2003; Yuan and Harrison 2005; Chen et al. 2007). On the basis of characterisation of deformation-dependent permeability proposed by Yuan and Harrison (2005), we assume that a damaged rock element may be represented hydraulically as a volume of rock containing three orthogonal fractures. This representation is shown

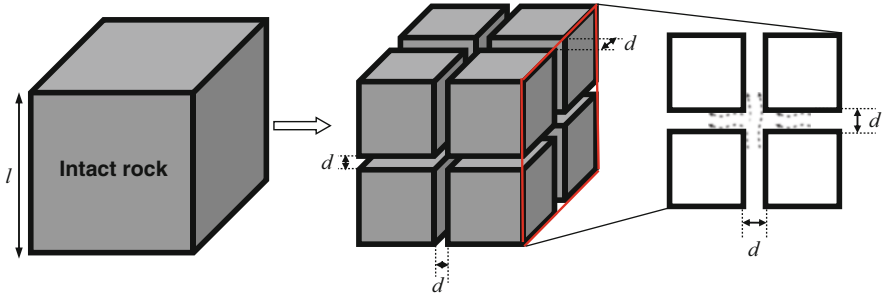


Fig. 8.5 Schematic illustration of permeability of a rock element due to brittle failure

conceptually in Fig. 8.5. Assuming that the three fractures are planar and have parallel sides, the aperture of the fractures is given approximately by

$$d \approx \frac{\Delta V}{3l^2} \approx \frac{\varepsilon_v V}{3\sqrt[3]{V^2}} = \frac{\varepsilon_v \sqrt[3]{V}}{3} \quad (8.16)$$

where ΔV is the volume change of the element due to dilatation, and l is the side length of the element before dilatation. The so-called cubic law gives the flow rate between smooth parallel plates as

$$q = \frac{d^3 \rho_l g}{12\mu_l} \frac{\Delta H}{l} \quad (8.17)$$

where ΔH is the fluid (water) head loss across the two ends. In Eq. 8.17, the hydraulic conductivity is given by the term $d^2 \rho_l g / 12\mu_l$. Therefore, the hydraulic conductivity for a damaged rock element (when $D > 0$) can be expressed as

$$k_d = \frac{d^2 \rho_l g}{12\mu_l} = \frac{\sqrt[3]{V^2} \rho_l g}{108\mu_l} \varepsilon_v^2 \quad (8.18)$$

In RFPA3D, Eq. 8.18 is employed to represent the permeability variation for a damaged rock element.

8.3 Numerical Implementation and System Design

8.3.1 Numerical Implementation

Consider isotropic elasticity constitutive relation, FEM format involves the 6×6 matrix \mathbf{D}_{ed} represents the unrolling of the fourth-order tensor, its value depends on the degree of damage,

$$\mathbf{D}_{ed} = E_0(1 - D) \begin{bmatrix} \frac{(1-\nu)}{(1+\nu)(1-2\nu)} & \frac{\nu}{(1+\nu)(1-2\nu)} & \frac{\nu}{(1+\nu)(1-2\nu)} & 0 & 0 & 0 \\ & \frac{(1-\nu)}{(1+\nu)(1-2\nu)} & \frac{\nu}{(1+\nu)(1-2\nu)} & 0 & 0 & 0 \\ & & \frac{(1-\nu)}{(1+\nu)(1-2\nu)} & 0 & 0 & 0 \\ & & & \frac{1}{2(1+\nu)} & 0 & 0 \\ & \text{symm} & & & \frac{1}{2(1+\nu)} & 0 \\ & & & & & \frac{1}{2(1+\nu)} \end{bmatrix} \quad (8.19)$$

In 3D FE modelling of RFPA, the used computation element is an eight-node hexahedron element, which is the smallest unit cell for analysis, i.e., RVE. The detailed derivation process and relevant expressions of strain and stress fields can be found in Zienkiewicz and Taylor (2005)'s work.

8.3.2 System Design

In view of the user-friendly graphical user interface (GUI) of the PC and the powerful computing capacity of the HPC cluster, the PC and the HPC cluster are used to deal with the pre- and post-processing parts and the parallel solving part, respectively, in RFPA. Figure 8.6 presents the flowchart of parallel computing in RFPA with the PC and cluster platforms, respectively. At the hardware layer, a server-client architecture is used, with the PC as the client and the cluster as the server for parallel computing. At the software layer, computation is executed through cooperation between different modules running in the Windows and Linux operating systems. As a listener working on the cluster, the client will set up a communication link with the server platform. Firstly, a GUI program, the Visual C++ language for Windows, is employed to prepare the pre-processing data files, i.e. the pre- and post-processing modules (see Fig. 8.6). When these data files are ready, the server accepts the request through the socket module, files are then uploaded to the cluster through the network. Then, the parallel FEM solver in the cluster, developed in the FORTRAN 95 language for Linux, reads these files, solves the problem, produces and integrates the corresponding result files. Finally, the result files are copied and uploaded to the PC by a data transfer program on the cluster platform. The damage analysis module is then executed and the results are displayed by the PC. Hence, the entire parallelization work focuses only on the most time-consuming FE solving process. The pre- and post-processing parts are still dealt with by the serial version in the PC. The advantages of PC and cluster platforms, as well as different operating systems (Windows and Linux), are fully utilized.

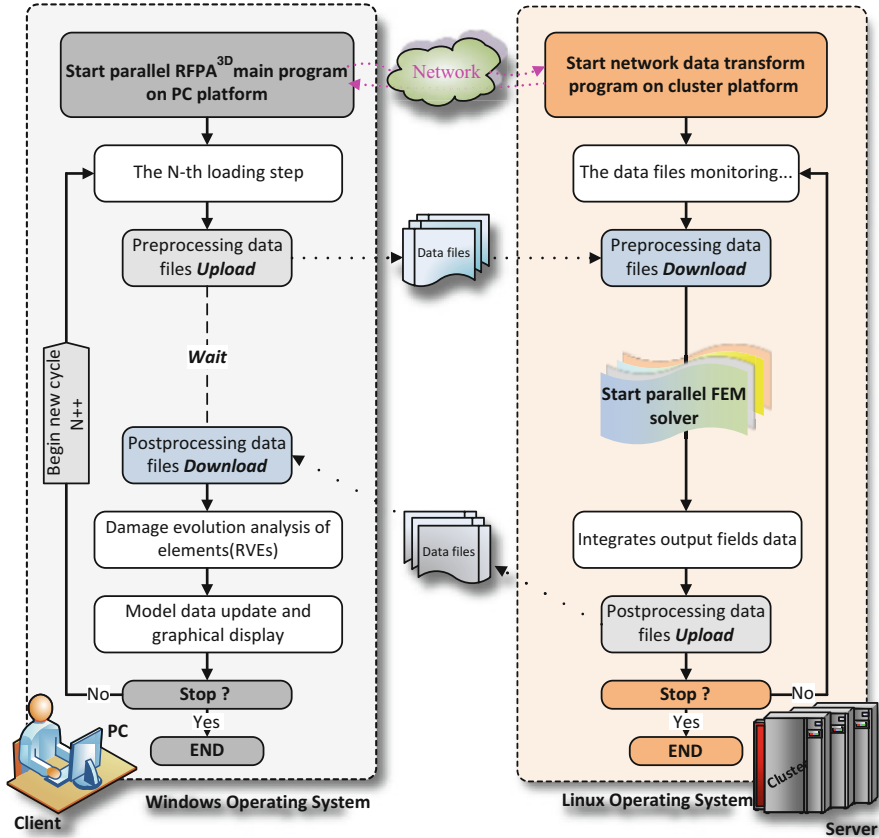


Fig. 8.6 Flowchart of parallel computing in RFPA with PC and cluster platform

8.4 Numerical Results

8.4.1 Verification

To verify the accuracy of the improved FSD model and the capability of RFPA, we simulated a three-dimensional cylindrical specimen with that was 45 mm in length and 20 mm in diameter. In the simulation with RFPA3D, a generated crack has the width of an element. To reflect realistically the crack propagation in a rock sample, a large number of elements are necessary in the simulation (Aliabadi 1999). The cylindrical specimen is discretised into 680,000 elements. Constant upstream and downstream fluid pressures of 3.5 MPa and 1.5 MPa, respectively, are applied to the bottom and top of the sample as shown in Fig. 8.7.

We numerically compress this sample vertically to simulate damage. The input parameters used in the model are selected to simulate a heterogeneous and brittle

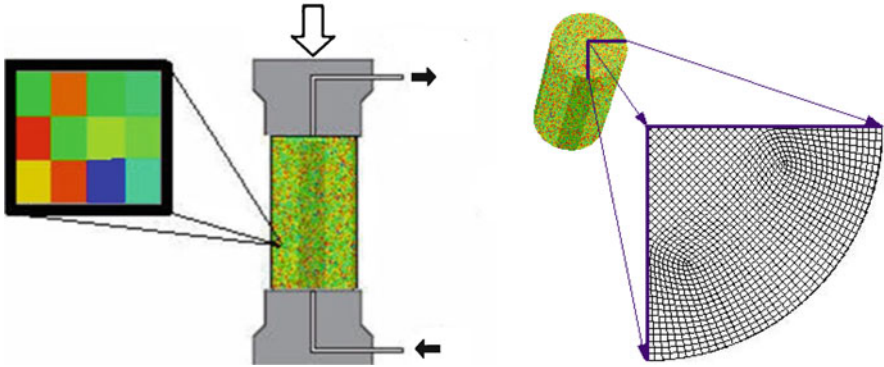


Fig. 8.7 Model setup for numerical simulation on the failure process of rock sample subject to hydro-mechanical loading and sample configuration and meshes

Table 8.1 Rock properties

Parameters	Value	Unit
Homogeneity index (m)	2.0	
Young's modulus (E_0)	22 GPa	GPa
Compressive strength (f_c)	120 MPa	MPa
Poisson's ratio (ν)	0.25	
Internal friction angle (φ)	30	°
Uniaxial tensional strength (f_t)	12	MPa
Permeability coefficient (k_0)	1e-8	cm/s
Coefficient of pore-water pressure (α)	0.8	
Coupling coefficient (β)	0.1	

rock and are reported in Table 8.1. Figure 8.8 shows the numerically obtained relationships between stress-strain and permeability variation. Figure 8.9 shows the numerically simulated progressive failure process. The simulation results compare well with experimental results (Fig. 8.9e). Initially, deformation is elastic, and permeability appears to decrease with compressive loading. As the axial strain increases to stage B, localised degradation (representing the onset of microcracking) begins to occur as specific elements attain their peak strengths. In stage A-B, these isolated flaws propagate, as expected, in the direction parallel to the maximum principal stress. This effect has been observed in numerous well-documented laboratory tests. In stage B-C, the permeability increases until yielding, leading to a significant increase in permeability. Therefore, the permeability increase is due to the microfractures connected by isolated flaws within the sample. In other words, the macroscopic flow behaviour depends not only on local permeability variations but also on the connectivity of the more conductive elements.

Figure 8.10 is the final fracture mode in a different section of the simulation. One can clearly observe the crack configurations, including the length, angle and density.

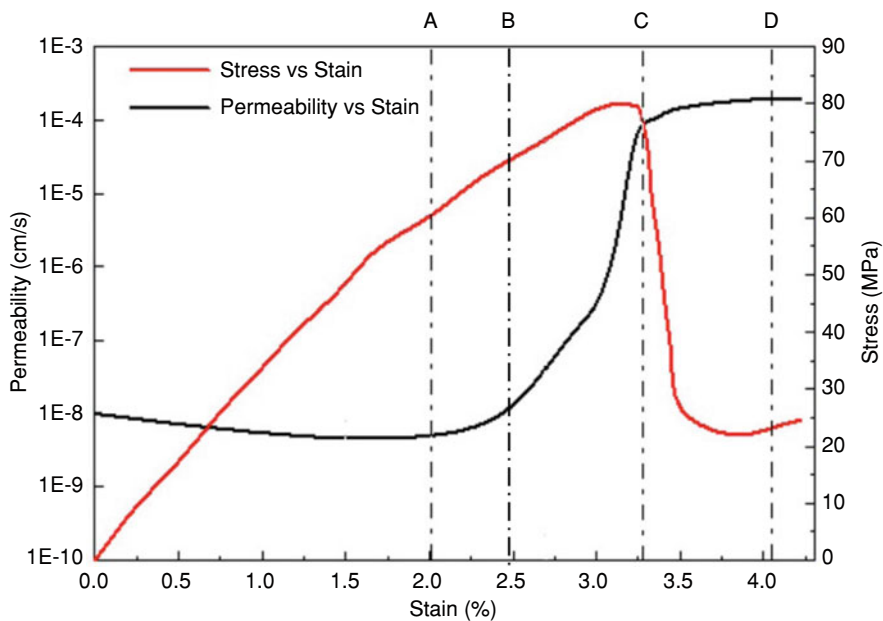


Fig. 8.8 Numerically obtained relationship among stress, permeability and strain of the sample

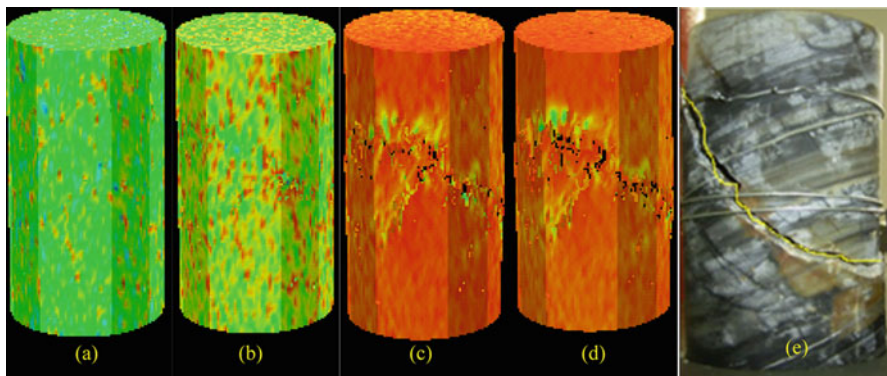


Fig. 8.9 Failure process of sample: (a–d) numerical results (Different colour reflects stress fields); (e) experimental failure mode

The failure planes are not theoretical 60° from horizontal direction due to the mesoscopic heterogeneity. In sections D1 and D3, the number of macrofractures is limited, while both macrofractures and isolated flaws (microfractures) are very abundant where section D2 intersects the primary fracture surface.

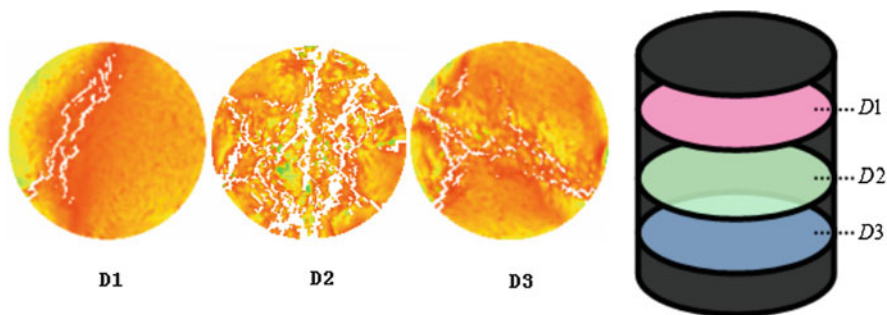


Fig. 8.10 Fracture pattern at different section in the sample

8.4.2 Applications

8.4.2.1 Hydraulic Fracturing Behaviour at Different Confining Pressures

The success or failure of hydraulic fracturing technology is largely dependent on the design of fracture configurations and the optimisation of treatments compatible with the in-situ conditions of a given reservoir. The in-situ stress is the primary factor in determining the orientation of propagating hydraulic fractures. A small-scale model is used to investigate the behaviour of the fracturing away from the wellbore under different stress regimes, as shown in Fig. 8.11. A wellbore with a diameter of 40 mm is assumed to be located at the centre of a 1000 mm × 1000 mm × 1200 mm block. The block was discretised into 1,200,000 elements (100 × 100 × 120). A perforated section (which is subjected to hydraulic pressure) is located in the centre of the wellbore. Hydraulic pressure is applied along the boundary of the interior hole in the perforated section at an initial pressure of 8.5 MPa. The rate of pressurisation increase is kept constant throughout the numerical tests at 0.05 MPa/step.

It is assumed that the fluid is Newtonian and that the rock formation is permeable. Three different cases are simulated to illustrate the influence of the far-field stress on the hydraulic fracturing behaviour. The applied confining stresses, representing the effect of the far-field stresses, are reported in Table 8.2, and the borehole axis is aligned with one of the in-situ stress directions. The mechanical parameters used in the modelling are reported in Table 8.3.

Figure 8.12a shows the evolution of pore pressure during the hydraulic fracturing process for case I (at section X = 500 mm). Generally, there is no preferential location along the wellbore wall for the fracture to initiate because the geometry of the sample is symmetrical and the magnitudes of the far-field stresses σ_x and σ_y are equal. Therefore, the location and orientation of the fracture initiation is unpredictable. However, the macroscale orientation of the fractures is horizontal, i.e., the fractures formed in a plane perpendicular to the Z axis.

Fig. 8.11 Model configuration

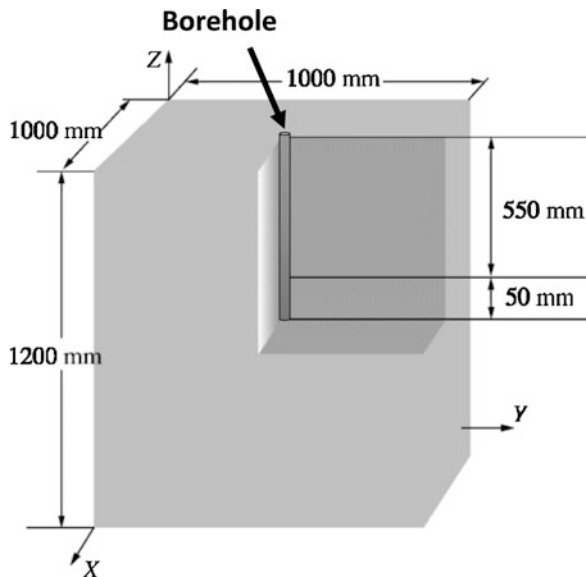


Table 8.2 Confining pressures

Case	σ_x (MPa)	σ_y (MPa)	σ_z (MPa)
I	4.0	4.0	1.0
II	1.0	3.0	5.0
III	1.0	1.0	1.0

Table 8.3 Rock properties

Parameters	Value	Unit
Homogeneity index (m)	4.0	
Young’s modulus (E_0)	6 GPa	GPa
Compressive strength (f_c)	100 MPa	MPa
Poisson’s ratio (ν)	0.25	
Internal friction angle (φ)	30	°
Uniaxial tensional strength (f_t)	10	MPa
Permeability coefficient (k_0)	1e-5	cm/s
Coefficient of pore-water pressure (α)	0.8	
Coupling coefficient (β)	0.01	

Figure 8.12b, c show the numerical results for cases II and III, respectively. The pressure for fracture initiation for all three cases is approximately 10 MPa, which is close to the theoretical value based on elasticity, although there is a small error induced by the heterogeneity of the materials. On the basis of the numerical results, one can conclude that the propagation of the hydraulic fractures is controlled by the far-field stress orientation. The hydraulic fracture selects the path of least resistance through the material, and the random locations of the individual heterogeneities result in an irregular hydraulic fracture trajectory. In reality, a perfect transverse fracture (i.e., a perfectly planar fracture perpendicular to any stress direction) is not possible in highly heterogeneous reservoir rock.

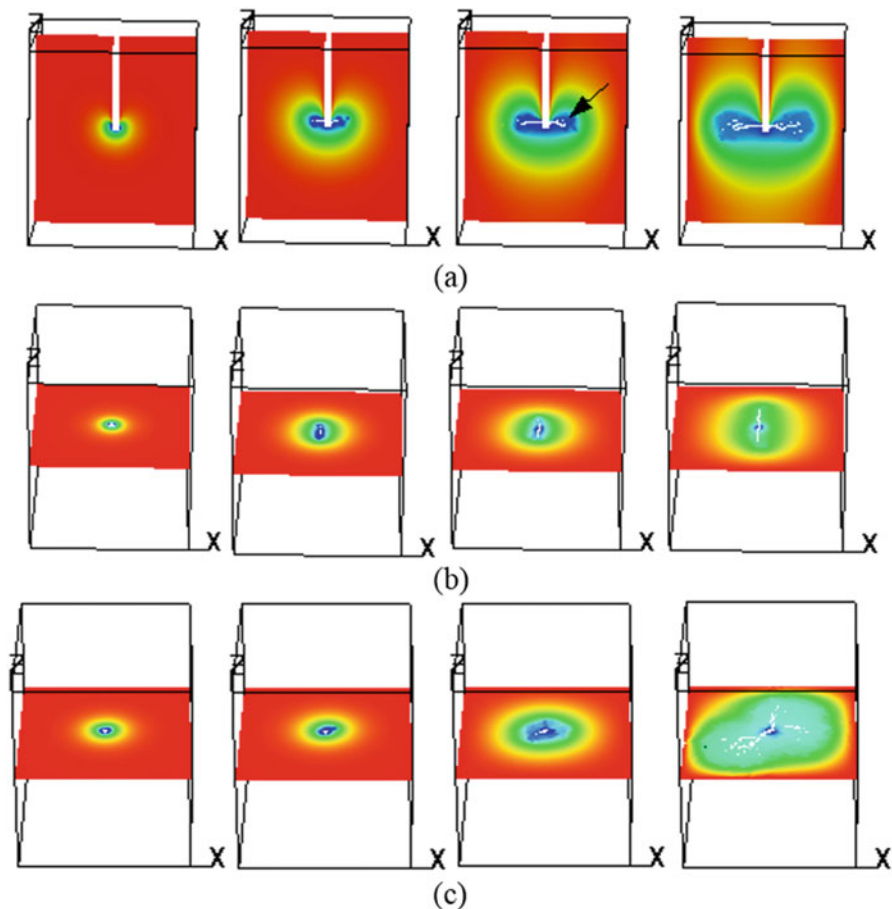


Fig. 8.12 Hydraulic fracturing process of Case I, II and III. The blue color represents the distribution of water pressure. (a) hydraulic fracturing mode of Case I, (b) hydraulic fracturing mode of Case II, (c) hydraulic fracturing mode of Case III

As soon as the fracture propagates slightly out of plane, the shear stress component reorients the fracture towards the preferred direction for fracture propagation with minimum resistance. For example, although the cracks in case I and II initiated and propagated in a plane, they branched out after growing for a short distance. Isolated fractures also open within the rock mass. Such fractures generate from weak elements. Despite these fractures, cases I and II represent two typical fracture modes in hydraulic fracturing process, as shown in Fig. 8.13. The numerically obtained fracture pattern closely resembles experimentally observed hydraulic fracture paths (Meng et al. 2010; Deng et al. 2004).

Case III shows multiple major fracture traces that are formed without any preferred orientations. The traces show significant branching and isolated fracturing. Because the magnitudes of the far-field stress in x , y , and z direction are identical to

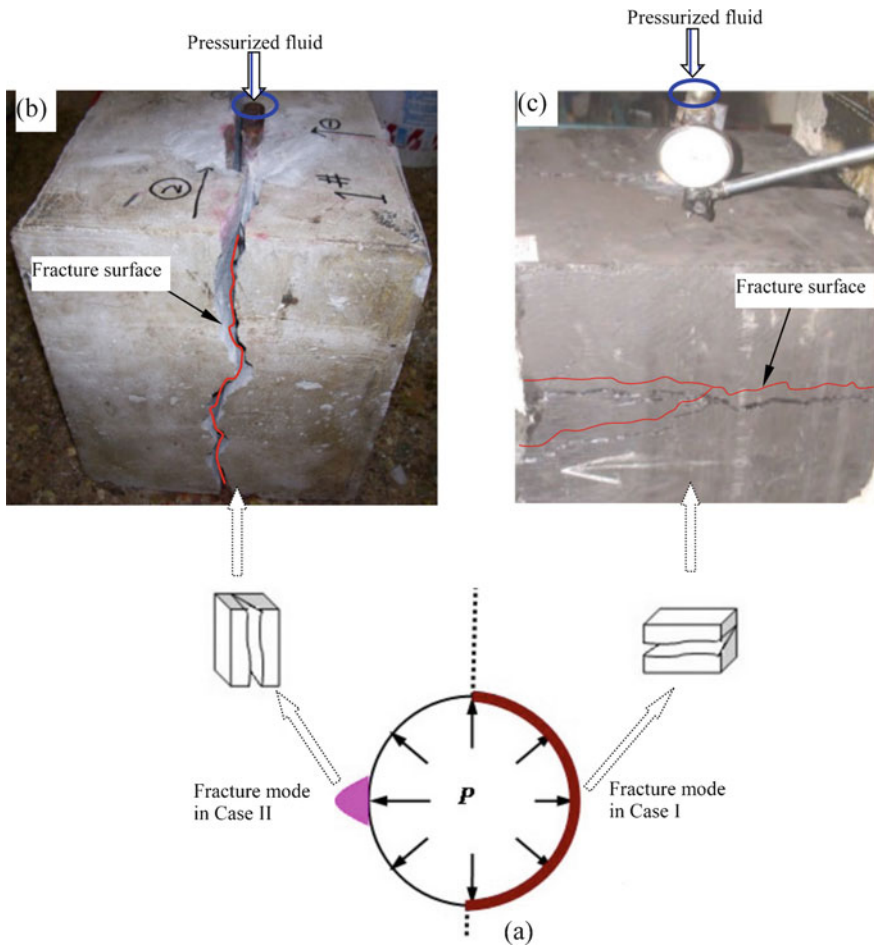


Fig. 8.13 Sketch of the effect of stress state on fracture mode: (a) the typical mode of fractures initiated from wellbore (Economides and Nolte 2000), (b) fracture parallel to wellbore (Meng et al. 2010), (c) fracture perpendicular to wellbore. (Deng et al. 2004)

each other, the crack pattern in this case depends completely on the local heterogeneity. Much of the energy from the hydraulic pressure was consumed by the branching of the fractures. Detournay and Carbonell (1994) noted that fractures always propagate unstably at slow pressurisation rates and uniform far-field stress conditions. The breakdown pressures for cases I, II and III are 10.7 MPa, 11.25 MPa and 11.45 MPa, respectively. The greater the difference in the magnitude of the far-field stresses, the lower the hydraulic pressure for the propagation of fractures will be.

Figure 8.14 shows the corresponding fracture modes for the three cases, mostly tension. The visualisation of complex fracture growth along the non-preferred direction illustrates the physical phenomena that lead to increasing injection pressure and decreasing fracture volume.

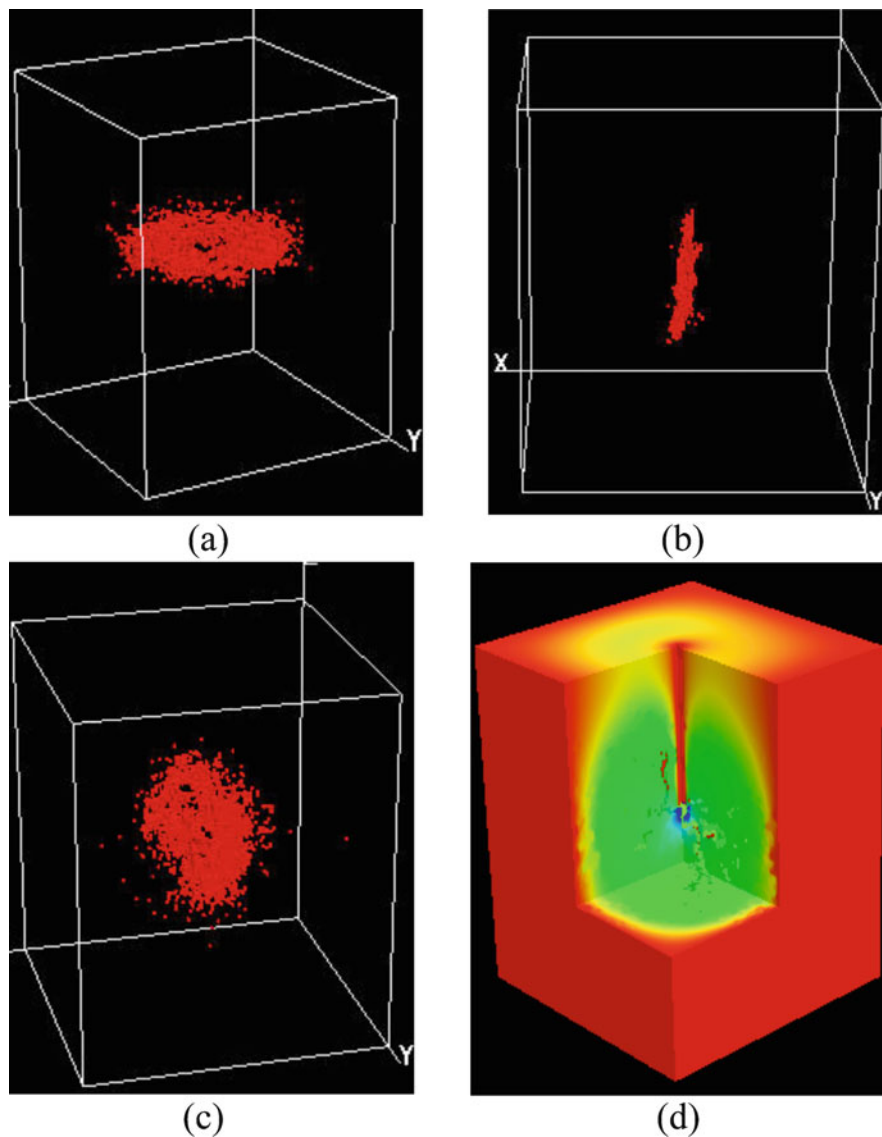


Fig. 8.14 Spatial distribution of fractures: (a) Case I, (b) Case II, (c) Case III and (d) Case III-fracture mode in the section planes cutting through well bore

8.4.2.2 Hydraulic Fracturing Behaviour in Multiple Rock Layers

Fluid-driven or hydraulic fractures, either natural or man-made, that propagate vertically in horizontally layered rocks may interact with interfaces and intersect different layers. To illustrate the complexity and the challenges involved in

modelling hydraulic fractures in multi-layer strata, a conceptual model is employed, as shown in Fig. 8.15. The model contains six rock layers with varying stiffnesses and permeabilities, and the interfaces between the layers are assumed to be perfectly bonded. Layer No. 2 and No. 5 are assumed to be pay zone layers, and the lower pay zone layer (No. 5) is selected to be hydraulically fractured. An 8 m-high perforated section is located in the centre of layer No. 5. Hydraulic pressure is applied along the boundary of the interior hole in the perforated section. Initial stresses of $\sigma_x = 5.0MPa$, $\sigma_y = 5.0MPa$, and $\sigma_z = 10.0MPa$ are applied on the outer boundaries of the model. The model has been discretised into 1,200,000 elements ($100 \times 100 \times 120$). The physico-mechanical parameters employed in the calculation are reported in Table 8.4. To investigate the effect of the rock strata properties on the fracturing mode, another two cases (cases II and III) were considered. In case II, the elastic modulus and strength properties are assumed to be reduced by 10%, compared with those of case I, while in case III, the elastic modulus and strength properties are reduced by 20%, compared with those of case I. The other parameters were kept constant in cases II and III.

The numerically simulated fracturing mode is shown in Fig. 8.16, and the corresponding fracturing mode is shown in multiple views in Fig. 8.17. The pressure gradient is increased for a relatively narrow fracture channel that carries the relatively high flow rate. The initiation and propagation of fractures are generally restricted within the pay zone layer, although a few isolated short fractures (flaws) appear in the covering layer. One should note that there is an intact layer between the pay zone layer and the covering layer, which indicates that the fracture in the pay zone layer did not propagate into the covering layer. The randomly distributed short fractures in the covering layer are formed within the weakest elements, where the

Fig. 8.15 Model configuration

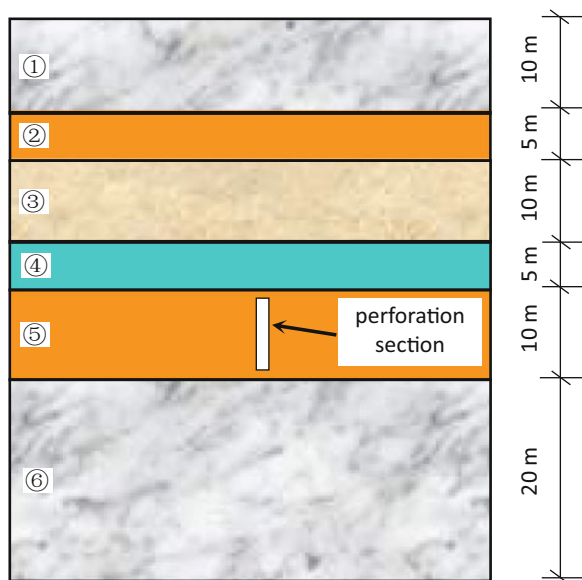


Table 8.4 Physico-mechanical parameters for Case I

Rock layer	Young's modulus E_0 /GPa	Compressive Strength f_c /MPa	Tensile strength f_t /MPa	Internal cohesive angle $\varphi/(\text{°})$	Poisson's ratio ν	Density $\rho/(\text{kN}\cdot\text{m}^{-3})$	Hydraulic conductivity $k_0/(\text{cm}\cdot\text{s}^{-1})$	Coefficient of pore-water pressure (α)
①	40	100	10	35	0.20	26	1e-7	0.9
②, ⑤	30	40	4	30	0.30	25	1e-5	0.9
③	25	35	3.5	30	0.30	25	1e-7	0.9
④	15	30	3	30	0.30	25	1e-7	0.9
⑥	30	60	6	30	0.25	26	1e-7	0.9

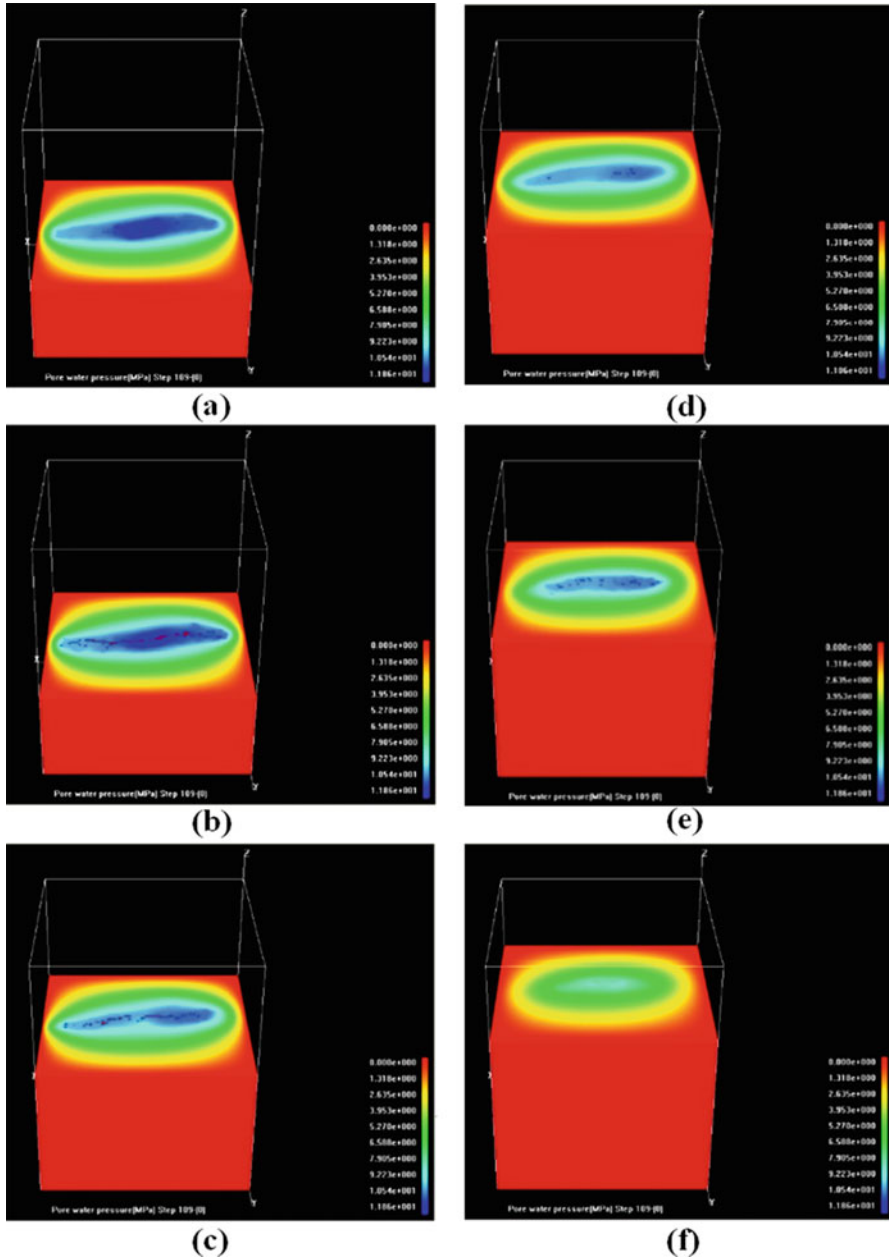


Fig. 8.16 Configuration of hydraulic fractures for Case I at different section along Z-axial. (a) $Z = 20$ m, (b) $Z = 25$ m, (c) $Z = 30$ m, (d) $Z = 32$ m, (e) $Z = 35$ m, (f) $Z = 45$ m

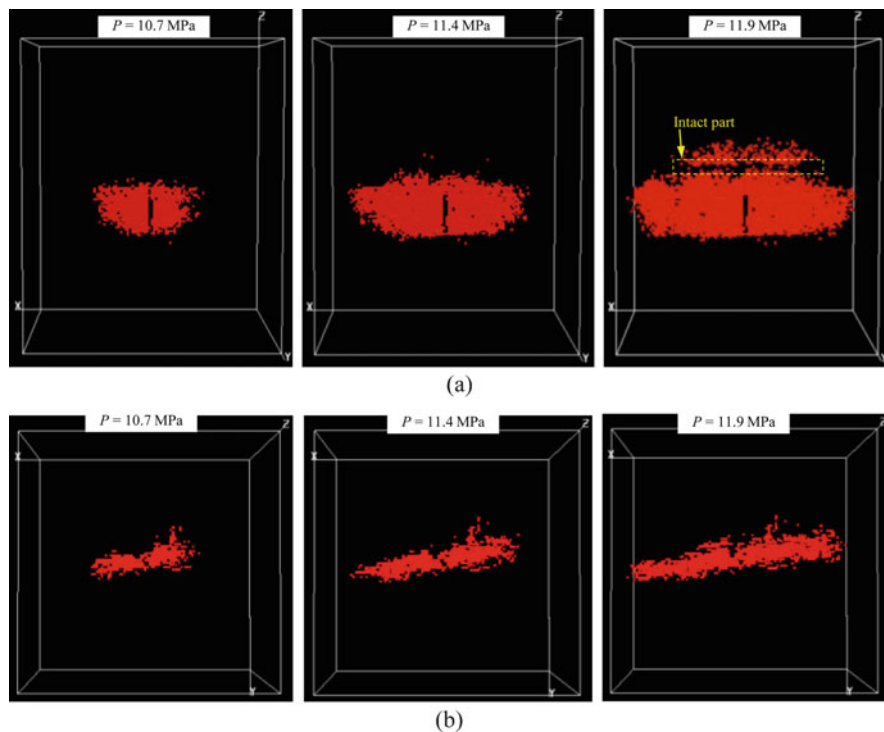


Fig. 8.17 Numerically obtained hydraulic fracturing mode of Case I: (a) side view in Y-Z plane, and (b) overlooking view in X-Y plane

local tensile stress reaches the local tensile strength. The tensile stress results mainly from the local pore pressure (the rock formation is assumed to be permeable) and the contrasts in the elastic properties of the involved strata. Therefore, the arrangement of these isolated short fractures is concordant with the direction of the macrofracture in the pay zone layer. As such, only a primary fracture, and no distinct fracture branches and offsets, forms in the pay zone layer.

Figures 8.18 and 8.19 show the fracturing modes for case II and case III, respectively. The fluid-driven fractures clearly propagate across the interfaces from the pay zone layer to adjacent layers and continue to propagate. By overcoming the higher vertical stress and the extra compressive stress generated from the interaction between the fractures, each fracture is initiated in a non-preferred direction, turns and twists during propagation, and tends to align itself with the preferred direction and plane. Of all three cases, the results from case III are the most disappointing because the length of the fracture in the pay zone layer is short while most of fractures propagate into the adjacent layers.

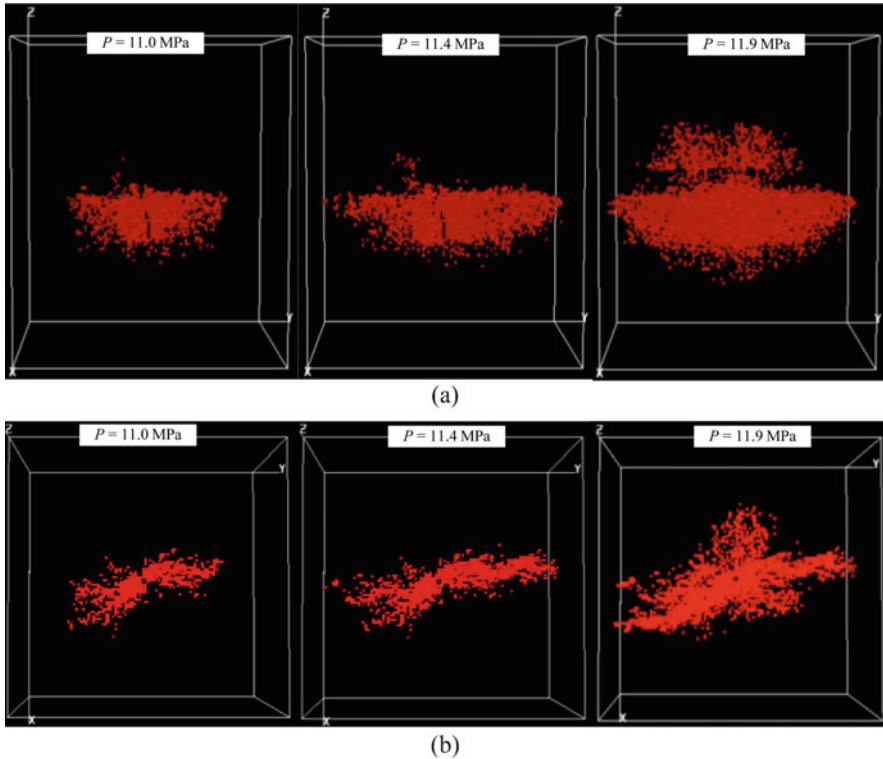


Fig. 8.18 Numerically obtained hydraulic fracturing mode of Case II: (a) side view in Y–Z plane, and (b) overlooking view in X–Y plane

The results indicate that the material properties, Young's modulus and strength can influence fracture propagation. According to the elasticity considerations applied to perfectly bonded interfaces or strong interfaces, a fracture that initiates in the stiffer of the two layers is able to advance towards and enter the softer layer but is not able to grow from the soft layer to the stiff layer (Erdogan and Biricikoglu 1973; Helgeson and Aydin 1991; Zhang et al. 2007). If the adjacent layer has a higher Young's modulus than that of the layer with the fracture, the strain energy decreases as the fracture tip approaches the interface, and propagation will be impeded. For the opposite case, the strain energy will be enhanced, and the fracture continues to propagate across the interface and into the intact adjacent layer. Compared with case I, stronger adjacent rock layers with higher toughnesses are found to efficiently resist fracture propagation from the pay zone layers.

Because the stress barrier near the interface is weak because of the flexibility of the intact soft layer, the local heterogeneity is more likely to induce out-of-plane fracture growth (Mofazzal Hossain and Rahman 2008). In reality, the rock formation

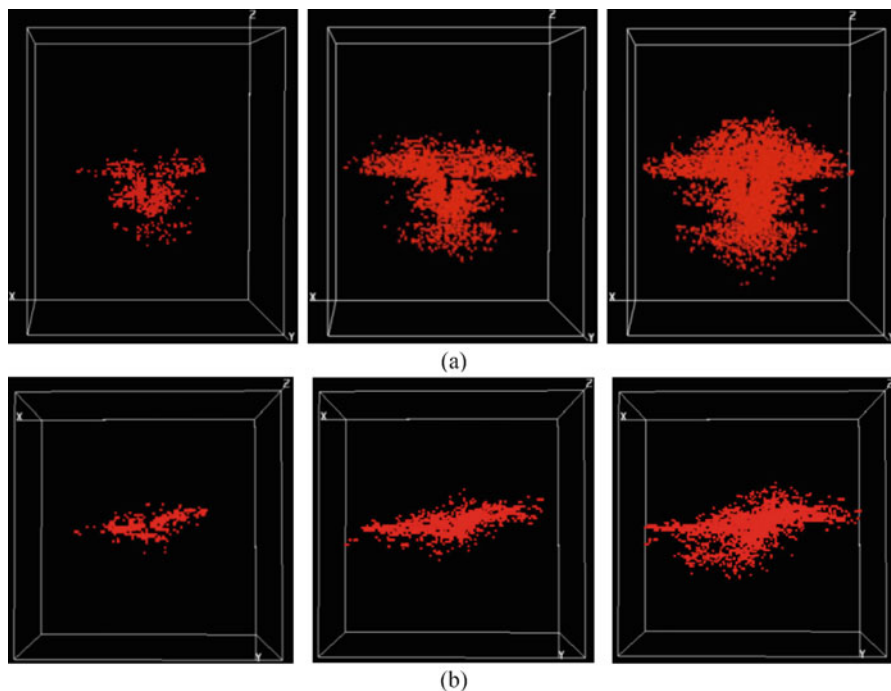


Fig. 8.19 Numerically obtained hydraulic fracturing mode of Case III: (a) side view in Y–Z plane, and (b) overlooking view in X–Y plane

in the field is extremely heterogeneous. The variation in failure mode is highly sensitive to the local features of the rock mass. As a result, the fracture surface is rough, and mixed-mode fracture propagation further affects the non-planar fracture growth in the non-preferred direction. In reality, there are two types of failure, high-stress failure and low-strength failure, for different materials. In a homogeneous material, failure begins at the high-stress site whereas, in a heterogeneous material (e.g., rock), failure may start at the weaker locations because of the presence of pores, microfractures, and grain boundaries. This observation led Fairhurst (1964) to introduce the notion of “stress severity”, which represents the ratio of the theoretical stress at the moment of failure to the stress that would theoretically be necessary for failure at any given point. Heterogeneity is the main reason for failures that occur in locations where the stress is not necessarily the greatest.

8.5 Summary

In this study, a finite element program, RFPA, is developed for coupled fracture modelling. The constitutive law of this model considers strength and stiffness degradation, stress-dependent permeability for the pre-peak stage, and deformation-dependent permeability for the post-peak stage. The hydraulic fracturing process inside a rock specimen is numerically simulated using this model. Three coupled processes are considered: (i) mechanical deformation of the solid medium that is induced by the fluid pressure acting on the fracture surfaces and the rock skeleton, (ii) flow of fluid within the fracture, and (iii) propagation of the fracture.

Then, 3D modelling of progressive failure and associated fluid flow in heterogeneous rocks was used to investigate the hydro-mechanical response of the rock specimen at the scale of typical laboratory samples. And, the 3D modelling of the hydraulic fracturing process was conducted.

Although natural cases are often much more complex than the numerical models considered here, the study highlights some interesting phenomena for complex hydraulic fracturing in rock masses. Using the present FSD model and RFPA code, many factors associated with hydraulic fracturing engineering will be considered in the future.

References

- Aliabadi MH (1999) Fracture of rock. Computational Mechanics Publications, WITPRESS, Boston/Southampton
- Chen YF, Zhou CB, Sheng YQ (2007) Formulation of strain-dependent hydraulic conductivity for a fractured rock mass. *Int J Rock Mech Min Sci* 44:981–996
- Deng GZ, Wang SB, Huang BX (2004) Research on behavior character of crack development induced by hydraulic fracturing in coal-rockmass. *Chin J Rock Mech Eng* 23(20):3489–3493
- Detournay E, Carbonell R (1994) Fracture mechanics analysis of breakdown process in minifrac or leak-off tests. In: Proc., Eurock'94. Balkema, Rotterdam, pp 399–407
- Economides MJ, Nolte KG (2000) Reservoir stimulation. Willey, Singapore
- Erdogan F, Biricikoglu V (1973) Two bonded half planes with a fracture going through the interface. *Int J Eng Sci* 11:745–766
- Esmaili K, Hadjigeorgiou J, Grenon M (2010) Estimating geometrical and mechanical REV based on synthetic rock mass models at Brunswick Mine. *Int J Rock Mech Min Sci* 47(6):915–926
- Fairhurst C (1964) On the validity of the Brazilian test for brittle materials. *Int J Rock Mech Min Sci* 1:535–546
- Fang Z, Harrison JP (2002) Development of a local degradation approach to the modelling of brittle fracture in heterogeneous rocks. *Int J Rock Mech Min Sci* 39:443–457
- Feng XT, Pan PZ, Zhou H (2006) Simulation of the rock microfracturing process under uniaxial compression using an elasto-plastic cellular automaton. *Int J Rock Mech Min Sci* 43(7):1091–1108
- Helgeson DE, Aydin A (1991) Characteristics of joint propagation across layer interfaces in sedimentary rocks. *J Struct Geol* 13:897–911

- Jaeger JC, Cook NGW, Zimmerman RW (2007) *Fundamentals of rock mechanics*, 4th edn. Blackwell, Oxford
- Li G, Tang CA (2015) A statistical meso-damage mechanical method for modelling trans-scale progressive failure process of rock. *Int J Rock Mech Min Sci* 74:133–150
- Li SP, Wu DX (1997) Effect of confining pressure, pore pressure and specimen dimension on permeability of Yin Zhuang sandstone. *Int J Rock Mech Min Sci* 34:435–441
- Liang ZZ, Xing H, Wang SY, Williams DJ, Tang CA (2012) A three-dimensional numerical investigation of the fracture of rock specimens containing a pre-existing surface flaw. *Comput Geotech* 45:19–33
- Lisjak A, Grasselli G, Vietor T (2014a) Continuum-discontinuum analysis of failure mechanisms around unsupported circular excavations in an isotropic clay shales. *Int J Rock Mech Min Sci* 65:96–115
- Lisjak A, Tatone BSA, Grasselli G, Vietor T (2014b) Numerical modelling of the anisotropic mechanical behaviour of opalinus clay at the laboratory-scale using FEM/DEM. *Rock Mech Rock Eng* 47(1):187–206
- Liu HY, Kou SQ, Lindqvist PA, Tang CA (2004) Numerical studies on the failure process and associated microseismicity in rock under triaxial compression. *Tectonophysics* 384:149–174
- Ma GW, Wang XJ, Ren F (2011) Numerical simulation of compressive failure of heterogeneous rock-like materials using SPH method. *Int J Rock Mech Min Sci* 48(3):353–363
- Meng QM, Zhang SC, Guo XM, Chen XH, Zhang Y (2010) A primary investigation on propagation mechanism for hydraulic fracture in glutenite formation. *Int J Oil Gas Coal Technol* 32(4):119–123
- Otto S, Till P, Hartmut K (2001) Development of damage and permeability in deforming rock salt. *Eng Geol* 61:163–180
- Pearce CJ, Thavalingam A, Liao Z, Bicanic N (2000) Computational aspects of the discontinuous deformation analysis framework for modeling concrete fracture. *Eng Fract Mech* 65:283–298
- Pietruszczak S, Xu G (1995) Brittle response of concrete as a localization problem. *Int J Solids Struct* 32:1517–1533
- Potyondy DO, Cundall PA (2004) A bonded-particle model for rock. *Int J Rock Mech Min Sci* 41(8):1329–1364
- Shao JF, Zhou H, Chau KT (2005) Coupling between anisotropic damage and permeability variation in brittle rocks. *Int J Numer Anal Methods Geomech* 29:1231–1247
- Shen WQ, Shao JF, Gatmiri B (2012) A micro-macro model for clayey rocks with a plastic compressible porous matrix. *Int J Plast* 36(9):64–85
- Stormont JC, Daemen JJK (1992) Laboratory study of gas permeability changes in rock salt during deformation. *Int J Rock Mech Min Sci Geomech Abstr* 29:325–342
- Susan E, Minkoff C, Mike S, Steve B (2003) Coupled fluid flow and geomechanical deformation modeling. *J Pet Sci Eng* 38:37–56
- Tang CA (1997) Numerical simulation on progressive failure leading to collapse and associated seismicity. *Int J Rock Mech Min Sci* 34(2):249–261
- Tang CA, Kaiser PK (1998) Numerical simulation of cumulative damage and seismic energy release in unstable failure of brittle rock-part I. *Fundamentals*. *Int J Rock Mech Min Sci* 35(2):113–121
- Tang CA, Tham LG, Lee PKK, Yang TH, Li LC (2002) Coupled analysis of flow, stress and damage (FSD) in rock failure. *Int J Rock Mech Min Sci* 39(4):477–489
- Weibull W (1981) A statistical distribution function of wide applicability. *J Appl Mech* 18:293–297
- Yuan SC, Harrison JP (2005) Development of a hydro-mechanical local degradation approach and its application to modelling fluid flow during progressive fracturing of heterogeneous rocks. *Int J Rock Mech Min Sci* 42:961–984
- Yuan SC, Harrison JP (2006) A review of the state of the art in modelling progressive mechanical breakdown and associated fluid flow in intact heterogeneous rocks. *Int J Rock Mech Min Sci* 43(7):1001–1022

- Zhang X, Jeffrey RG, Thiercelin M (2007) Deflection and propagation of fluid-driven fractures at frictional bedding interfaces: a numerical investigation. *J Struct Geol* 29:396–410
- Zhang W, Chen JP, Yuan XQ, Xu PH, Zhang C (2013) Analysis of RVE size based on three-dimensional fracture numerical network modelling and stochastic mathematics. *Q J Eng Geol Hydrogeol* 46:31–40
- Zhao GF, Fang J, Zhao J (2010) A 3D distinct lattice spring model for elasticity and dynamic failure. *Int J Numer Anal Methods Geomech* 35(8):859–885
- Zhou XP, Yang HQ (2012) Multiscale numerical modeling of propagation and coalescence of multiple cracks in rock masses. *Int J Rock Mech Min Sci* 55:15–27
- Zhu WC, Tang CA (2004) Micromechanical model for simulating the fracture process of rock. *Rock Mech Rock Eng* 37(1):25–56
- Zhu WL, Wong TF (1997) The transition from brittle faulting to cataclastic flow: permeability evolution. *J Geophys Res* 102(B2):3027–3041
- Zhu QZ, Kondo D, Shao JF, Pensee V (2008) Micromechanical modelling of anisotropic damage in brittle rocks and application. *Int J Rock Mech Min Sci* 45(4):467–477
- Zienkiewicz OC, Taylor RL (2005) *The finite element method for fluid dynamics*, 6th edn. Elsevier Butterworth- Heinemann, Oxford